Electronic Supplementary Information

Study on the Relationship between Magnetic Field and Dielectric Properties in Two Ferromagnetic complexes

Li Yang,[a] Jing Li,[a] Tian-Cheng Pu,[b] Ming Kong,[a] Jing Zhang[a] & You Song*[a]

[a] *State Key Laboratory of Coordination Chemistry, Collaborative Innovation Center of Advanced Mirostructures, School of Chemistry and Chemical Engineering, Nanjing University, Nanjing 210093, China.*

[b] *Department of Chemical and Biomolecular Engineering, John Hopkins University, Baltimore, Maryland 21218, United States*

Caption of Content

1. **Table S1.** Metal–Ligand Bond Lengths (Å) and Angles (°) in Complex **1**.
2. **Table S2.** Metal–Ligand Bond Lengths (Å) and Angles (°) in Complex **2**.
3. **Fig. S1** Plot of χ_M^{-1} *vs T* for **1**. The solid line represents the best−fit curve following Curie-Weiss law.
4. **Fig. S2** Plot of χ_M^{-1} *vs T* for **2**. The solid line represents the best−fit curve following Curie-Weiss law.
5. **Fig. S3** Plot of *M vs H* for **1** and **2** at 2 K**.**
6. **Fig. S4** Temperature dependence of the real ε' part of the dielectric permittivity in the case of no field and different external field for **1**.
7. **Fig. S5** Temperature dependence of the real ε' part of the dielectric permittivity in the case of no field and different external field for **2**.
8. **Fig. S6** The model of dielectric permittivity measurements for **1** and **2** under an applied magnetic field.
9. **Fig. S7** Details of the IR spectra corresponding to spectral range 500-3500 cm^{-1} for (a) **1** and (b) **2**.
10. **Fig. S8** Frequency dependence of (a) the real ε' part and (b) the imaginary ε'' of the dielectric permittivity for **1**
11. **Fig. S9** Frequency dependence of (a) the real ε' part and (b) the imaginary ε'' of the dielectric permittivity for **2**.
12. **Fig. S10** Arrhenius plots of ln(τ) vs the inverse temperature T^{-1} under an applied magnetic field of 1020 G for **1** and **2**. Red lines show the fit of data to the Arrhenius expression $\tau = \tau_0 \exp(E_a / k_B T)$.
13. **Fig. S11** Arrhenius plots of ln(τ) vs the inverse temperature T^{-1} under an applied magnetic field of 2200 G for **1** and **2**. Red lines show the fit of data to the Arrhenius expression $\tau = \tau_0 \exp(E_a / k_B T)$.
14. **Fig. S12** Arrhenius plots of ln(τ) vs the inverse temperature T^{-1} under an applied magnetic field of 3500 G for **1** and **2**. Red lines show the fit of data to the Arrhenius expression $\tau = \tau_0 \exp(E_a / k_B T)$.
15. **Fig. S13** Cole-Cole diagram of **1** (a) and **2** (b), plotted using χ_M' and χ_M'' at different temperature. The solid lines represent the fits to a general Debye model.

Table S1. Metal–Ligand Bond Lengths (Å) and Angles (°) in Complex **1**.

Cr1–O1^{i}	1.9796(11)	Cr1–O1^{iv}	1.9796(11)	Fe1–O2^{vii}	2.1174(13)
Cr1–O1^{ii}	1.9796(11)	Cr1–O1^{v}	1.9796(11)	Fe1–O2^{viii}	2.1175(13)
Cr1–O1^{iii}	1.9796(11)	Fe1–O2	2.1174(13)	Fe1–O2^{ix}	2.1175(13)
Cr1–O1	1.9796(11)	Fe1–O2^{vi}	2.1174(13)	Fe1–O2^{x}	2.1175(13)
O1^{i}–Cr1–O1^{ii}	180.00	O1^{i}–Cr1–O1^{v}	88.92(5)	O2^{vii}–Fe1–O2^{ix}	88.76(8)
O1^{i}–Cr1–O1^{iii}	91.08(5)	O1^{ii}–Cr1–O1^{v}	91.08(5)	O2–Fe1–O2^{x}	93.10(6)
O1^{ii}–Cr1–O1^{iii}	88.92(5)	O1^{iii}–Cr1–O1^{v}	180.0	O2^{vi}–Fe1–O2^{ix}	93.10(6)
O1^{i}–Cr1–O1	88.92(5)	O1^{iv}–Cr1–O1	180.0	O2^{vii}–Fe1–O2^{ix}	88.76(8)
O1^{ii}–Cr1–O1	91.08(5)	O2–Fe1–O2^{viii}	85.09(7)	O2^{viii}–Fe1–O2^{ix}	93.10(6)
O1^{iii}–Cr1–O1	88.92(5)	O2–Fe1–O2^{ix}	177.48(7)	O2–Fe1–O2^{x}	93.10(6)
O1^{i}–Cr1–O1^{iv}	91.08(5)	O2^{vi}–Fe1–O2^{ix}	93.11(6)	O2^{vi}–Fe1–O2^{x}	177.47(7)
O1^{ii}–Cr1–O1^{iv}	88.92(5)	O2–Fe1–O2^{viii}	85.09(7)	O2^{vii}–Fe1–O2^{ix}	88.76(8)
O1^{iii}–Cr1–O1^{iv}	91.08(5)	O2^{vi}–Fe1–O2^{viii}	93.10(6)	O2^{viii}–Fe1–O2^{x}	88.76(8)

Symmetry codes: (i) y−1, −x+y, −z; (ii) −y+1, x−y+2, z; (iii) x−y+1, x+1, −z; (iv) −x, −y+2, −z; (v) −x+y−1, −x+1, z; (vi) −y+1, −x+1, −z+1/2; (vii) −x+y, −x+1, z; (viii) x, x−y+1, −z+1/2; (ix) −x+y, y, −z+1/2; (x) −y+1, x−y+1, z; (xi) −y+1, x−y, z; (xii) −x+y+1, −x+1, z.

Table S2. Metal–Ligand Bond Lengths (Å) and Angles (°) in Complex **2**.

Cr1–O1	1.9753(15)	Cr1–O1^{xi}	1.9753(15)	Ni1–O2^{iv}	2.0530(16)
Cr1–O1^{viii}	1.9753(15)	Cr1–O1^{xii}	1.9753(15)	Ni1–O2^{v}	2.0530(16)
Cr1–O1^{ix}	1.9753(15)	Ni1–O2	2.0530(16)	Ni1–O2^{vi}	2.0530(16)
Cr1–O1^{x}	1.9753(15)	Ni1–O2^{iii}	2.0530(16)	Ni1–O2^{vii}	2.0530(16)
O1^{viii}–Cr1–O1^{x}	91.39(7)	O1^{viii}–Cr1–O1^{xii}	91.39(7)	O2^{iii}–Ni1–O2	176.63(10)
O1^{viii}–Cr1–O1^{ix}	180.00(8)	O1^{ix}–Cr1–O1^{xii}	88.61(7)	O2^{iv}–Ni1–O2^{vi}	93.20(7)
O1^{ix}–Cr1–O1^{x}	88.61(7)	O1^{x}–Cr1–O1^{xii}	91.39(7)	O2^{v}–Ni1–O2^{vi}	176.63(10)
O1^{viii}–Cr1–O1^{xi}	88.61(7)	O1^{xi}–Cr1–O1^{xii}	180.00(8)	O2^{iii}–Ni1–O2^{vi}	89.31(10)
O1^{ix}–Cr1–O1^{xi}	91.39(7)	O1–Cr1–O1^{xii}	88.61(7)	O2–Ni1–O2^{vi}	93.19(7)
O1^{x}–Cr1–O1^{xi}	88.61(7)	O2^{iv}–Ni1–O2^{v}	89.31(10)	O2^{iv}–Ni1–O2^{vii}	176.63(10)
O1^{viii}–Cr1–O1	88.61(7)	O2^{iii}–Ni1–O2^{iii}	84.40(10)	O2^{v}–Ni1–O2^{vii}	93.19(7)
O1^{ix}–Cr1–O1	91.39(7)	O2^{v}–Ni1–O2^{iii}	93.20(7)	O2^{iii}–Ni1–O2^{vii}	93.19(7)
O1^{x}–Cr1–O1	180.00(8)	O2^{iv}–Ni1–O2	93.20(7)	O2–Ni1–O2^{vii}	89.31(10)
O1^{xi}–Cr1–O1	91.39(7)	O2^{v}–Ni1–O2	84.40(10)	O2^{vi}–Ni1–O2^{vii}	84.40(10)

Symmetry codes: (i) −y+1, x−y, z; (ii) −x+y+1, −x+1, z; (iii) −y+1, −x+1, −z+1/2; (iv) −y+1, x−y+1, z; (v) −x+y, y, −z+1/2; (vi) −x+y, −x+1, z; (vii) x, x−y+1, −z+1/2; (viii) x−y+1, x, −z; (ix) −x+y+1, −x+2, z; (x) −x+2, −y+2, −z; (xi) −y+2, x−y+1, z; (xii) y, −x+y+1, −z.

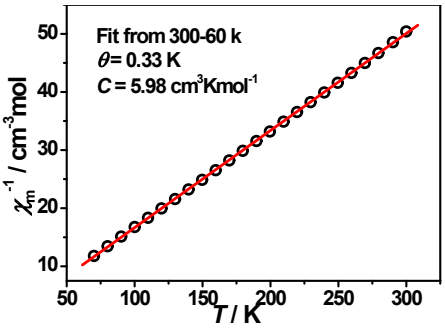

Fig. S1 Plot of χ_M^{-1} *vs T* for **1**. The solid line represents the best–fit curve following Curie-Weiss law.

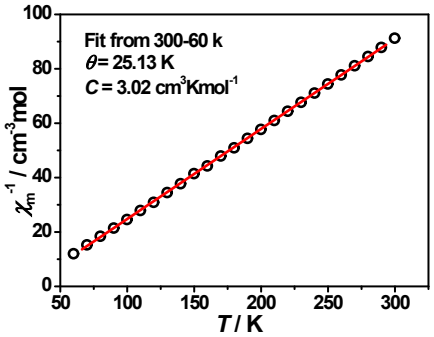

Fig. S2 Plot of χ_M^{-1} *vs T* for **2**. The solid line represents the best–fit curve following Curie-Weiss law.

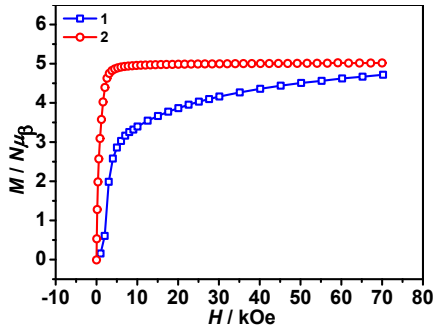

Fig. S3 Plot of *M vs H* for **1** and **2** at 2 K**.**

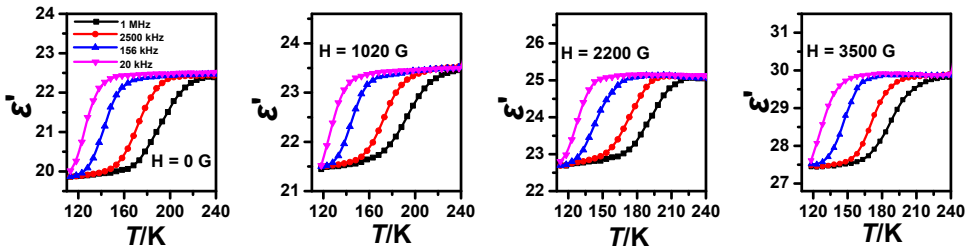

Fig. S4 Temperature dependence of the real *ε′* part of the dielectric permittivity in the case of no field and different external field for **1**.

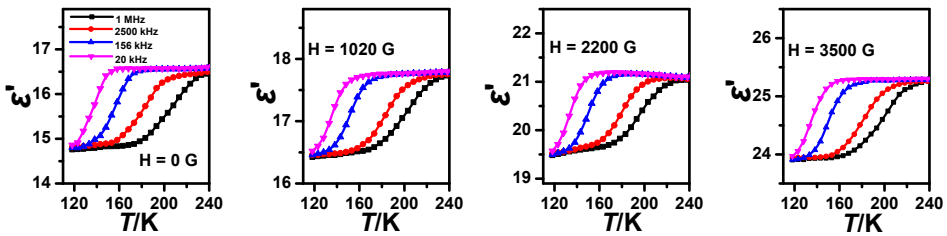

Fig. S5 Temperature dependence of the real *ε′* part of the dielectric permittivity in the case of no field and different external field for **2**.

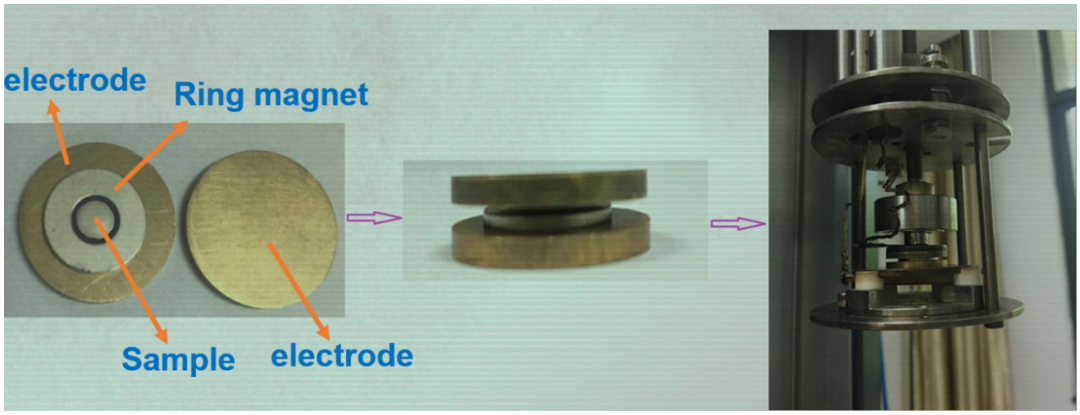

Fig. S6 The model of dielectric permittivity measurements for **1** and **2** under an applied magnetic field.

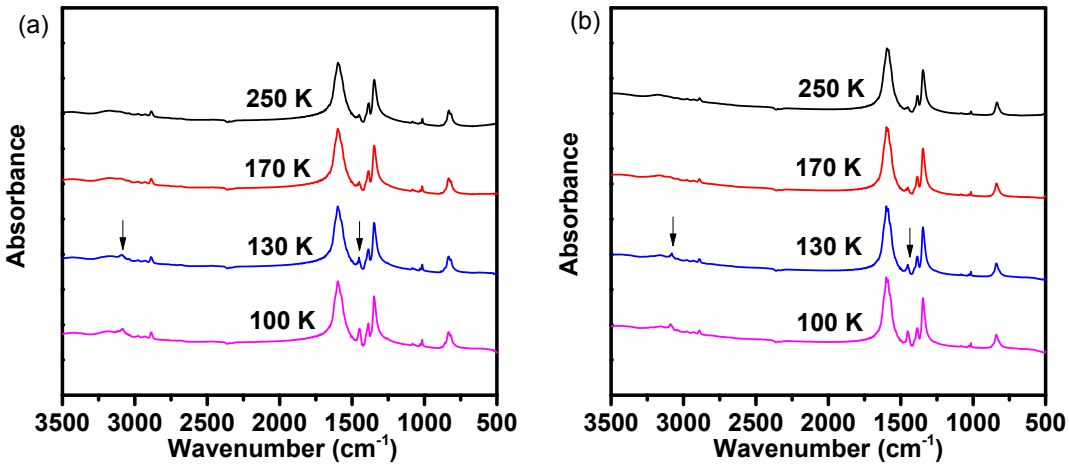

Fig. S7 Details of the IR spectra corresponding to spectral range 500-3500 cm^{-1} for (a) **1** and (b) **2**.

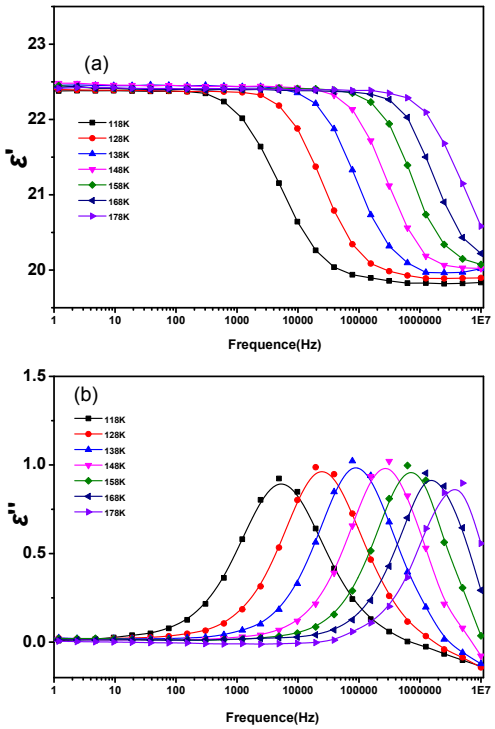

Fig. S8 Frequency dependence of (a) the real *ε′* part and (b) the imaginary *ε′′* of the dielectric permittivity for **1**.

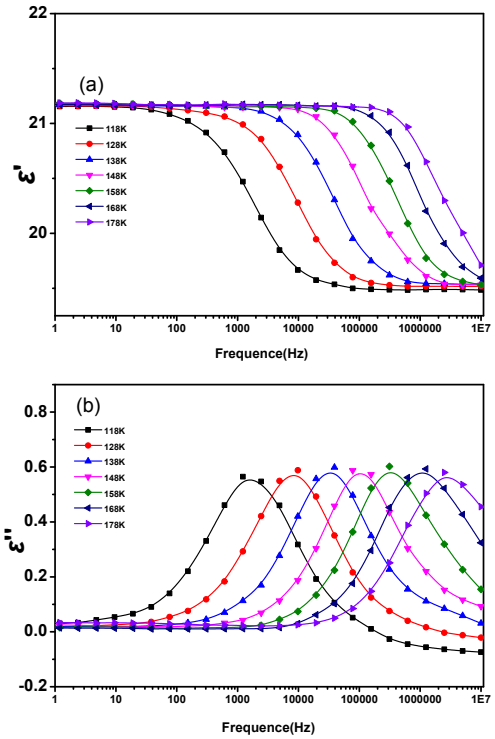

Fig. S9 Frequency dependence of (a) the real *ε′* part and (b) the imaginary *ε′′* of the dielectric permittivity for **2**.

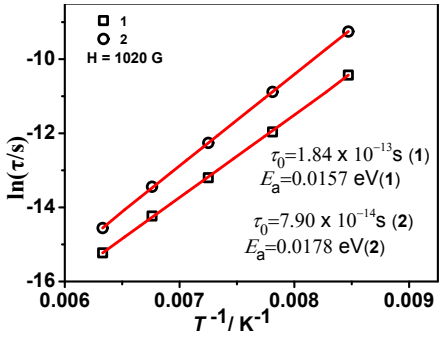

Fig. S10 Arrhenius plots of ln(τ) vs the inverse temperature T^{-1} under an applied magnetic field of 1020 G for **1** and **2**. Red lines show the fit of data to the Arrhenius expression $\tau = \tau_0 \exp(E_a / k_B T)$.

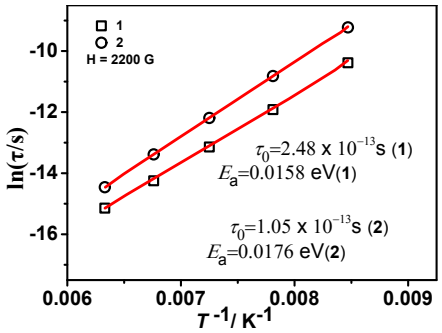

Fig. S11 Arrhenius plots of ln(τ) vs the inverse temperature T^{-1} under an applied magnetic field of 2200 G for **1** and **2**. Red lines show the fit of data to the Arrhenius expression $\tau = \tau_0 \exp(E_a / k_B T)$.

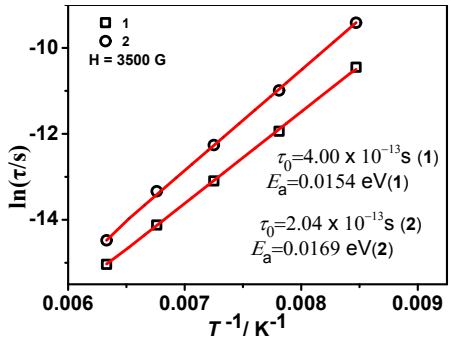

Fig. S12 Arrhenius plots of ln(τ) vs the inverse temperature T^{-1} under an applied magnetic field of 3500 G for **1** and **2**. Red lines show the fit of data to the Arrhenius expression $\tau = \tau_0 \exp(E_a / k_B T)$.

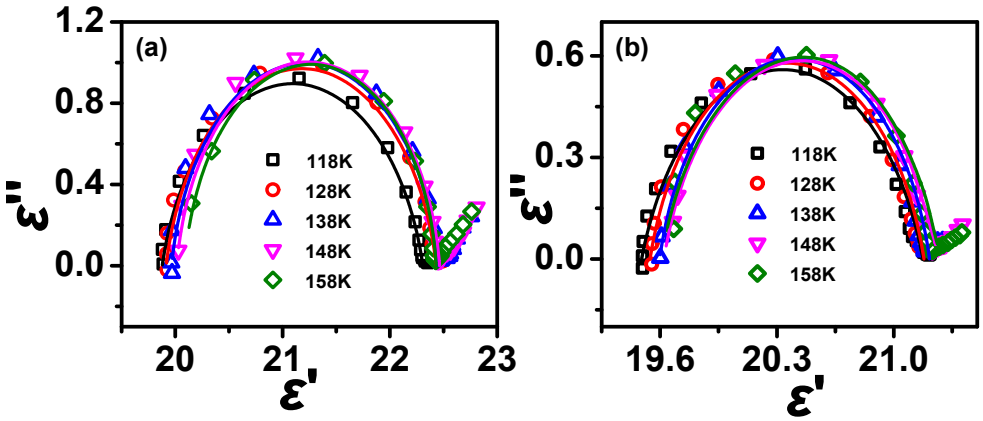

Fig. S13 Cole-Cole diagram of **1** (a) and **2** (b), plotted using χ_M' and χ_M'' at different temperature. The solid lines represent the fits to a general Debye model.